

## Collective electronic excitations in Ti and Zr and their dihydrides

I. V. Silkin,<sup>1</sup> I. P. Chernov,<sup>2</sup> V. M. Silkin,<sup>3,4,5</sup> and E. V. Chulkov<sup>3,4,6</sup>

<sup>1</sup>Laboratory of Nanostructured Surfaces and Coatings, Tomsk State University, pr. Lenina 46, 634050 Tomsk, Russia

<sup>2</sup>Engineering School of Nuclear Technology, Tomsk Polytechnic University, pr. Lenina 30, 634050 Tomsk, Russia

<sup>3</sup>Departamento de Física de Materiales, Facultad de Ciencias Químicas, Universidad del País Vasco, Apdo. 1072, 20080 San Sebastián/Donostia, Spain

<sup>4</sup>Donostia International Physics Center (DIPC), Paseo de Manuel Lardizabal 4, 20018 San Sebastián/Donostia, Spain

<sup>5</sup>IKERBASQUE, Basque Foundation for Science, 48011, Bilbao, Spain

<sup>6</sup>Centro de Física de Materiales CFM - Materials Physics Center MPC, Centro Mixto CSIC-UPV/EHU, Paseo de Manuel Lardizabal 5, 20018 San Sebastián/Donostia, Spain



(Received 18 May 2018; revised manuscript received 19 July 2018; published 7 August 2018)

Electron excitation spectra in Ti and Zr transition metals are calculated in the framework of time-dependent density functional theory. Several peaks found in the obtained loss functions are interpreted as collective excitations. The energy positions of the dominating bulk plasmons are in close agreement with the energy loss experiments. We investigated how the absorption of hydrogen modifies the dielectric properties of these materials. It is shown that the main plasmon energy blueshifts in a such process, again in agreement with experimental observations. On base of the calculated bulk dielectric functions of all these systems, we performed analysis of the excitation spectra at surfaces and nanoparticles. Several plasmon peaks in these systems with rather short lifetimes are found at reduced energies. It is shown how the nanoparticle excitation spectra are modified in the ultraviolet-frequency range upon hydrogen absorption.

DOI: [10.1103/PhysRevB.98.075111](https://doi.org/10.1103/PhysRevB.98.075111)

### I. INTRODUCTION

Hydrogen absorption in many metals results in formation of metal hydrides, which were intensively studied starting from the nineteenth century [1–5]. In particular, understanding how hydrogen interacts with transition metals is of significant scientific and technical interest since hydrogen penetrating into these materials results in strong modifications of its mechanical, electrical, optical, and other properties [6,7].

Thus a large number of experimental and theoretical studies on the Ti-H and Zr-H systems where the hydrogen content can vary relative to host metal (M) over a wide range of H composition reaching to a maximum capacity of H/M=2 have been reported. Weaver *et al.* [8] have carried out the photoelectron spectroscopy and synchrotron radiation study of TiH<sub>x</sub> and ZrH<sub>x</sub> systems to understand its electronic structure. The Ti-H and Zr-H phase diagrams were constructed [9,10]. First-principles calculations were used to characterize the bulk elastic properties of cubic and tetragonal phases of metal dihydrides to gain insight into the mechanical properties that govern the aging behavior [11]. The energetics and electronic properties of these hydrides have been studied in detail as well [12,13]. The electronic structure and lattice stability in the dihydrides of Ti and Zr were investigated in Refs. [14–16]. The stability of TiH<sub>2</sub> was addressed in Ref. [17] and analysis of partial composition of the electronic bands in TiH<sub>2</sub> was done in Ref. [18]. The phase transition of ZrH<sub>2</sub> from cubic to tetragonal structure has been theoretically investigated in Ref. [12].

Recently, several researchers have studied the total energy and electronic structure for Zr-H system [13,14]. Weiyi *et al.* [19] reported the structural and thermodynamic properties of ZrH<sub>2</sub>. The ground-state properties of ZrH<sub>2</sub> were studied by

Zhang *et al.* [20] using first-principles methods. The mechanical and structural stability of ZrH<sub>2</sub> were investigated by Wang *et al.* [21] using the plane-wave based pseudopotential method within the density functional theory framework. Yamanaka *et al.* [22] have reported the electronic, mechanical, electrical, and thermal characteristics of zirconium hydride and deuteride.

The hydrogenation of metals often leads to changes in optical and dielectric properties. This allows for fundamental studies of the hydrogenation process, as well as the exploration of various applications. Optical properties of hydrides are not always well-understood. For instance, still there are some questions in this regard for the  $\delta$ -TiH<sub>x</sub> ( $x = 2$ ) phase. The optical constants of TiH<sub>2</sub> were determined from the measurements on thin films in Ref. [23]. Apparently, they are different from the Ti optical data [24,25]. Optical properties of Zr were addressed in Ref. [26]. We are not aware of optical measurements in Zr hydrides except a recent experiment [27] performed for the low-content H phases demonstrating notable variation in plasmon energies with hydrogen variation.

Regarding the dielectric properties, numerous loss-energy experiments both on pure Ti and Zr and their hydrides were performed. Titanium and zirconium present a rich plasmonic structure with several well-defined plasmons. However, frequently, different interpretations for such loss peaks were offered in separate publications. Since there was no accompanying theoretical support, the question of interpretation of loss peaks in these metals is still open. As for the Ti and Zr hydrides, several measurements of loss spectra were realized as well. Strong variation with H absorption of energies of loss peaks was observed. However, first-principles calculations of collective excitations in these systems have not been done yet.

In this work, we perform a detailed study of the collective electronic excitation spectra of Ti and Zr in the framework of time-dependent density functional theory with full inclusion of the electronic band structure. From these calculations, we obtain information on the plasmon excitations in these metals. Performing similar calculations for  $\text{TiH}_2$  and  $\text{ZrH}_2$ , we investigate the impact of hydrogen absorption on the excitation spectra. On the basis of the calculated dielectric function of these materials, we evaluate the surface excitation spectra in the long-wavelength limit and find well-defined surface plasmons. Employing the Mie theory, we evaluate the excitation spectra for the nanoparticles. Our study presents quantitative data on the variation of the excitation spectra of titanium and zirconium upon the hydrogen uptake. We scrutinize the low-energy region very carefully in an attempt to find in the studied materials an acoustic-like plasmon which may exist in an electron system with two kinds of carriers with distinct Fermi velocities [28].

The rest of the paper is organized as follows. In Sec. II, we describe details of the *ab initio* calculation of the linear response dielectric and loss functions. The calculated results and their discussion are reported in Sec. III. The main conclusions of this work are presented in Sec. IV. Unless otherwise stated explicitly, atomic units ( $\hbar = e^2 = m_e = 1$ ) are used throughout the paper.

## II. CALCULATION DETAILS

Excitations in electron systems are characterized by a transferred momentum  $\mathbf{Q}$  and excitation energy  $\omega$ , which determine the dielectric function [29]. Working in reciprocal space, the microscopic dynamical nonlocal dielectric function  $\epsilon(\mathbf{r}, \mathbf{r}', \omega)$  can be expressed in a matrix form in terms of reciprocal lattice vectors  $\mathbf{G}$  and  $\mathbf{G}'$  and a transfer momentum  $\mathbf{q}$  from the first Brillouin zone (BZ) as  $\epsilon_{\mathbf{G}\mathbf{G}'}(\mathbf{q}, \omega)$ . The loss function  $L(\mathbf{Q}, \omega)$ , directly related to the spectra measured in the energy-loss experiments, is then given in terms of the dielectric function as

$$\begin{aligned} L(\mathbf{Q}, \omega) &\equiv -\text{Im}[\epsilon_{\mathbf{G}\mathbf{G}'}^{-1}(\mathbf{q}, \omega)] \\ &= -\text{Im}[1 + \nu(\mathbf{q} + \mathbf{G})\chi_{\mathbf{G}\mathbf{G}'}(\mathbf{q}, \omega)], \end{aligned} \quad (1)$$

where  $\mathbf{Q} = \mathbf{q} + \mathbf{G}$ ,  $\nu$  is the Coulomb potential, and  $\chi$  the density-response function of interacting electrons of the system. Within the time-dependent density functional theory (TDDFT) approach,  $\chi$  is given by a Dyson-type integral equation [30,31],  $\chi = \chi^0 + \chi^0(\nu + f_{\text{XC}})\chi$ . Here,  $\chi^0$  is the density-response function of the noninteracting electrons and the exchange and correlation kernel  $f_{\text{XC}}$  represents the functional derivative of the exchange-correlation potential with respect to electron density.

In a linear response theory, one can express the density-response function of noninteracting electrons,  $\chi^0$ , as a sum over independent transitions between one-particle states characterized by a wave function  $|n\mathbf{k}\rangle$  and energy  $\varepsilon_{n\mathbf{k}}$ . In reciprocal space, the imaginary part of  $\chi^0$  is expressed as

$$\begin{aligned} &\text{Im}[\chi_{\mathbf{G}\mathbf{G}'}^0(\mathbf{q}, \omega)] \\ &= \frac{2}{\Omega} \sum_{\mathbf{k}} \sum_{nn'}^{\text{BZ}} (f_{n\mathbf{k}} - f_{n'\mathbf{k}+\mathbf{q}}) \langle n\mathbf{k} | e^{-i(\mathbf{q}+\mathbf{G})\cdot\mathbf{r}} | n'\mathbf{k} + \mathbf{q} \rangle \\ &\quad \times \langle n'\mathbf{k} + \mathbf{q} | e^{i(\mathbf{q}+\mathbf{G}')\cdot\mathbf{r}} | n\mathbf{k} \rangle \delta(\varepsilon_{n\mathbf{k}} - \varepsilon_{n'\mathbf{k}+\mathbf{q}} + \omega). \end{aligned} \quad (2)$$

Here, the factor 2 accounts for spin,  $\Omega$  is a normalization volume, the sum over wave vectors  $\mathbf{k}$  is performed in the first BZ,  $n$  and  $n'$  are the energy-band indices, and  $f_{n\mathbf{k}}$  are the Fermi occupation factors.

The condition for the existence of collective excitations—plasmons—in bulk is  $\epsilon(\mathbf{Q}, \omega) = 0$  [29]. In the  $Q \rightarrow 0$  limit, the dielectric function  $\epsilon(\omega) = \epsilon_1(\omega) + i\epsilon_2(\omega)$  is relevant for bulk optical properties. Moreover, knowing this quantity, one may obtain the dielectric properties in finite systems. Thus the surface response function [32,33] is defined as  $g(\omega) = \frac{\epsilon(\omega)-1}{\epsilon(\omega)+1}$ . From the surface loss function defined as the imaginary part of  $g$ , one may obtain information about electronic excitations taking place at the surface. In particular, a condition for the existence of a surface plasmon is  $\epsilon = -1$  [34].

In case of a spherical particle in vacuum, its absorption spectrum in the Rayleigh limit is proportional to  $\text{Im}[\alpha]$ , where  $\alpha$  is the particle polarizability defined as  $\alpha(\omega) = \frac{\epsilon(\omega)-1}{\epsilon(\omega)+2}$ . This approximation is valid when the particle size is small in comparison with the light wavelength [35]. Collective charge oscillations in small particles occur with a frequency at which  $\epsilon = -2$ .

The above conditions for the existence of collective excitations in bulk, at surface, and in a particle can be only realized in an ideal electron gas system. In real materials due to unavoidable interband transitions, one should use a more soft condition. For instance, in a spherical particle, a maximum in the absorption occurs when  $\epsilon_1 = -2$ , due to the dipole plasma resonance of the spheres. The width and height of the resonance is determined by the value of  $\epsilon_2$  at the resonance.

Our starting point of the linear dielectric response calculations is the electronic band structure evaluated with density functional techniques within a plane-wave pseudopotential approach in the framework of the local density approximation for the ground-state calculations [36]. We use Bachelet, Hamann, and Schlüter type norm-conserving nonlocal ion pseudopotentials [37] for the description of electron-ion interaction. With these pseudopotentials, we achieve full convergence of the Kohn-Sham eigenvalues at a plane-wave cutoff of 80 Ry. The exchange-correlation potential is taken in the Ceperley-Alder form [38].

The calculations are based on the electronic structure obtained for  $\alpha$ -Ti and  $\alpha$ -Zr in hexagonal closed packed (h.c.p.) lattice. For Ti, we employ the experimental lattice parameters at room temperature  $a = 2.957$  and  $c = 4.685$  Å [39]. For Zr, we used  $a = 3.232$  and  $c = 5.147$  Å [40], which are very close to  $a = 3.233$  and  $c = 5.149$  Å measured recently [41].

The hydrogenation of these materials produces different hydrides like  $\xi$ ,  $\beta$ ,  $\gamma$ , and  $\delta$  phases at different conditions. The stoichiometric  $\delta$  phase of  $\text{TiH}_2$  and  $\text{ZrH}_2$  crystallizes into a  $\text{CaF}_2$ -like structure where the metal atoms occupy the face centered cubic (f.c.c.) lattice positions and hydrogen atoms reside at the tetrahedral interstitial positions [42]. The  $\text{TiH}_2$  hydride adopts the face centered tetragonal (f.c.t.) structure at low temperature and transforms into a f.c.c. phase above 310 K [43,44]. In this work, we studied the later system with a lattice parameter  $a = 4.454$  Å [45]. At ambient temperature and pressure, zirconium hydride crystallizes in a f.c.t. structure, whereas the f.c.c. fluorite type structure is considered as the metastable phase. In this work, for the  $\delta$ -Zr hydride, we

employed a f.c.c. structure with  $a = 4.802 \text{ \AA}$  corresponding to the volume of the f.c.t. phase [7,46]. This value is found to be close to that calculated in Ref. [47].

In Eq. (2), for the summation over the BZ, we employed a  $144 \times 144 \times 72 \text{ k}$  mesh in the case of Ti and Zr. A  $144 \times 144 \times 144 \text{ k}$  mesh was used in the calculations for  $\text{TiH}_2$  and  $\text{ZrH}_2$ . All occupied and unoccupied valence states with energies up to 50 eV above the Fermi level were included. In numerical calculations performed by using our own code [48], the  $\delta$  function in Eq. (2) was represented by a Gaussian with a broadening parameter of 25 meV. The real part of  $\chi^0$  was obtained from  $\text{Im}[\chi^0]$  via the Kramers-Kronig relation by numerical integration. For this, the  $\text{Im}[\chi^0]$  matrices were calculated on a discrete energy mesh in the 0–50 eV interval with a step of 5 meV.

In order to include crystal local-field effects (LFE) [49,50], we expand the  $\chi$ ,  $\chi^0$ , and  $\epsilon$  matrices over 100 vectors  $\mathbf{G}$ . Although the LFE may introduce strong variations in the excitation spectrum in some materials studied previously [51–58], we have checked that their role in the materials under study is rather modest.

In this work, we present the results obtained choosing the dynamical exchange-correlations kernel  $f_{\text{XC}}$  in a form of the time-dependent local-density approximation (TD-LDA) of Ref. [59]. We have checked that using a less elaborated kernel in the random-phase approximation (RPA) (when  $f_{\text{XC}} = 0$ ) introduces small quantitative changes in the excitation spectra of materials under study.

### III. CALCULATION RESULTS

#### A. Ti and Zr

##### 1. Band structure

The calculated electronic structure of Ti and Zr is reported in Fig. 1. In both metals, the energy bands present great similarity in the overall shape and are in agreement with the previous *ab initio* calculations [60–64]. In particular, one can see that the bottom of the valence states is formed from the *s*-like states, whereas the states lying in vicinity of the Fermi level are of the *d*-like type. Moreover, one can see that in both metals the Fermi level is crossed by several energy bands with different slopes resulting in different Fermi velocities. According to our

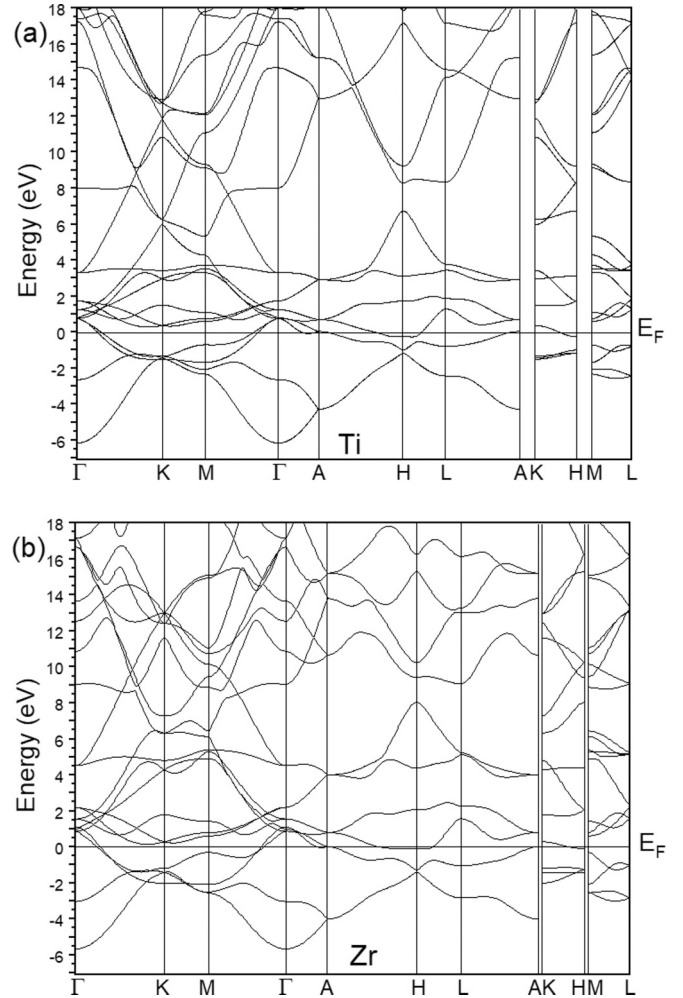


FIG. 1. Calculated band structure of Ti (a) and Zr (b) along some symmetry directions in the Brillouin zone. The energy is relative to the Fermi level  $E_F$  set to zero.

previous work [53–55], this suggests that in these materials might exist an acoustic-like mode corresponding to the out-of-phase collective oscillations of electron charge in different energy bands [28,65]. Although such a mode was not observed

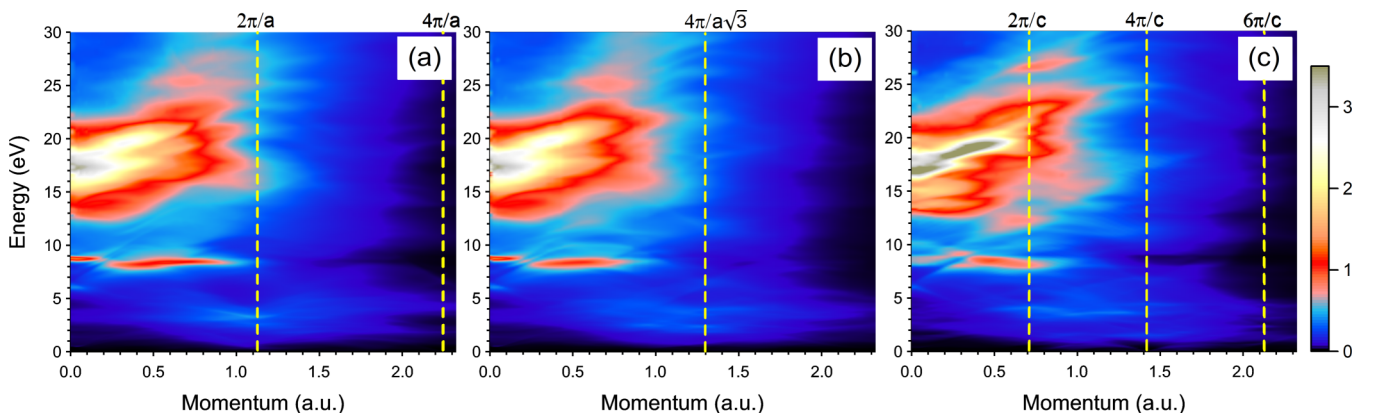


FIG. 2. Calculated loss function  $L(\mathbf{Q}, \omega)$  of Ti as a function of energy and momentum transfer  $\mathbf{Q}$  along  $\langle 100 \rangle$  (a),  $\langle 010 \rangle$  (b), and  $\langle 001 \rangle$  (c) symmetry directions of the h.c.p. lattice.

in a bulk material recently, a mode with a similar dispersion was detected at some metal surfaces [66–72].

## 2. Loss function

In Fig. 2, we present the loss function  $L(\mathbf{Q}, \omega)$  for Ti calculated at momentum transfers  $\mathbf{Q}$  along three main symmetry directions of the h.c.p. lattice. One can observe in Figs. 2(a) and 2(b) that at small momentum transfers the loss function in this material is dominated by a strong wide peak centered at the energy of 17.2 eV. In titanium, we find for momentum transfers in the hexagonal basal plane almost isotropic behavior of the excitation spectra since the loss function along the  $\langle 100 \rangle$  and  $\langle 010 \rangle$  symmetry directions is very similar. In both directions, upon momentum increase, the dominating plasmon peak shifts upward and can be traced as a well defined feature up to a momentum of about 1 a.u., although at lower momentum transfers it starts to split into several separate peaks. At larger momentum transfers, the loss function presents essentially a featureless behavior.

In the loss function along the  $\langle 001 \rangle$  direction reported in Fig. 2(c), one can also see a prominent plasmon peak with an energy of 16.9 eV at small momentum transfers. A second peak with slightly lower intensity is located at 18.0 eV. These peaks disperse upward with the momentum increase. Some differences can be noted in the excitation spectrum along this direction in comparison with those for the in-plane directions, although these differences are rather small. Along the  $\langle 001 \rangle$  direction, the plasmon peak can be distinguished up to  $Q \sim 1.1$  a.u. As seen in Fig. 2(c), before the plasmon peak ceases to exist at this  $Q$ , it starts to split into several separate peaks at lower momentum transfers, like it occurs in the other symmetry directions.

Close inspection of Fig. 2 reveals that several other features can be found in the loss function of Ti at small momentum transfers. In order to understand their nature in Fig. 3, we present  $\epsilon(\omega)$  and  $L(\omega)$  for two polarizations. In  $\epsilon_2$ , one can observe several peaks produced by numerous interband transitions involving the occupied and unoccupied states. The shapes of these peaks are different for these two polarizations revealing a notable anisotropy in this material. Presence of such peaks in  $\epsilon_2$  results in the strongly oscillating behavior of  $\epsilon_1$ . These oscillations in  $\epsilon_1$  are so pronounced that at some energies it crosses the zero line. As a result, in the in-plane loss function of Fig. 3(a), in addition to the conventional plasmon peak, three peaks at 0.5, 6.0, and 8.7 eV can be found. In the case of the 0.5 eV peak,  $\epsilon_1$  crosses the zero line accompanied by a presence of a local minimum in  $\epsilon_2$  in agreement with the optical measurements [73]. However, the intensity of the corresponding peak in the loss function is rather low since  $\epsilon_2$  is high in this energy interval. Regarding the 6.0 eV loss peak, we find that the real part of dielectric function although does not reach zero in the nearby region, it approaches this line rather closely. Therefore we interpret this feature as a plasmon. In the case of the 8.7 eV loss peak, since  $\epsilon_1$  crosses the zero line and  $\epsilon_2$  has a local minimum at fairly the same energies, we interpret this feature as a plasmon as well. The intensity of this mode is largest after the dominating 17.2 eV plasmon. Moreover, the 8.7 eV loss peak is rather narrow signaling that the lifetime of

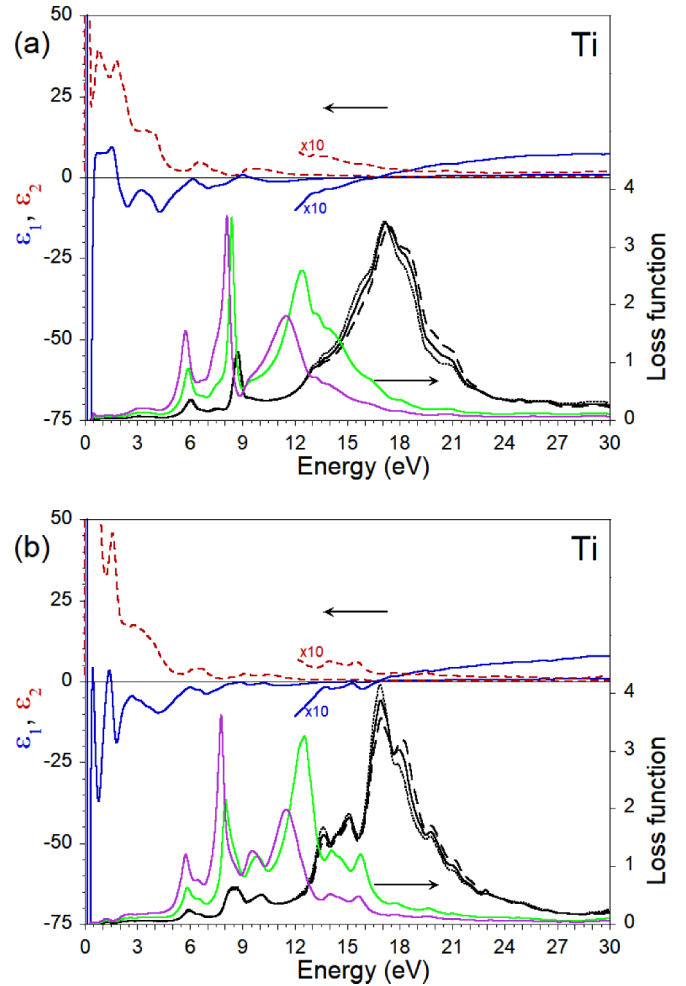


FIG. 3. Dielectric function  $\epsilon(\mathbf{Q}, \omega)$  and loss function  $L(\mathbf{Q}, \omega)$  in Ti calculated for (a) in-plane ( $Q = 0.009$  a.u.) and (b) out-of-plane ( $Q = 0.010$  a.u.) polarizations. Blue solid and red dashed lines show the real and imaginary parts of  $\epsilon$ , respectively. Black dotted lines show  $L$  calculated in the RPA and without inclusion of the LFE. Black long dashed lines represent  $L$  obtained in the RPA and the LFE included. Black, green, and magenta solid curves present bulk  $L(\omega)$ , surface  $\text{Im}[g(\omega)]$ , and particle  $\alpha(\omega)$ , respectively, evaluated in the TD-LDA framework with inclusion of the LFE.

this mode is rather long. Indeed, the width of this peak is the lowest one in comparison with that of all other modes. As seen in Figs. 2(a) and 2(b), along the  $\langle 100 \rangle$  and  $\langle 010 \rangle$  directions, the 8.7 eV peak is almost dispersionless up to  $Q = 0.2$  a.u. After that, it disappears and reappears again in the  $0.25 < Q < 1.0$  a.u. range at slightly lower energy. Again, in this momentum region, this peak has a fairly flat dispersion.

In the out-of-plane  $\epsilon_1(\omega)$  of Fig. 3(b), we observe an even larger number of the zero crossings. However, some of them, like those with energies below 2 eV, do not produce appreciable peaks in the loss function and the corresponding modes are effectively damped. Among them, a peak at 1.2 eV has some spectral weight only. At larger energies, we can detect peaks in the loss function at 6.0, 8.5, and 10.1 eV. It is difficult to interpret the 6.0-eV peak as a plasmon since in the nearby momentum region  $\epsilon_1$  does not reach the zero line and has

a local maximum at about  $-2$ . In this direction, the 8.5-eV loss peak is significantly broader in comparison to the in-plane polarization. It can be explained by the fact that  $\epsilon_1$  does not reach the zero line although approaches it very closely. As seen in Fig. 2(c) in the  $\langle 001 \rangle$  direction, this mode reappears at  $Q = 0.35$  a.u. and it is dispersionless up to about  $Q = 1.0$  a.u. At larger momentum transfers, in this energy range, we do not find any notable feature in the loss function of Ti. A peak at 10.1 eV in the loss function of Fig. 3(b) is difficult to interpret as a plasmon since  $\epsilon_1$  does not exceed  $-0.5$  at this energy. In contrast, the peaks at 13.6 and 15.2 eV can be interpreted as plasmons since  $\epsilon_1$  is very close to zero in this energy region. Nevertheless, we did not include these peaks in the list of plasmons in Ti since their intensity is relatively low in comparison with that of the main plasmon peak centered at 16.9 eV. The *ab initio* calculation [74] revealed notable anisotropy in the optical properties of Ti which can be related to the differences in the dielectric function and excitation spectra found here.

In Fig. 3, we add the loss function curves obtained in the RPA with and without inclusion of the local-field effects. The main effect of neglecting the LFE consists in the downward shift of all peaks in the loss function. However, the effect depends on the direction. Thus in the in-plane loss function of Fig. 3(a), the shift is about 0.2 eV for the main plasmon peak. At the same time, the peaks with lower energies are not affected notably by the LFE. The same occurs for the peaks with energies below 12 eV in the out-of-plane direction of Fig. 3(b). Moreover, the energy positions of the 13.6, 15.2, and 16.9 eV peaks are not modified by the LFE. The LFE change the intensity of these peaks only. The notable impact of the LFE on the loss function in this direction is the energy shift by 0.2 eV of the weak 18.0 eV peak. From comparison of black long-dashed and solid curves in Fig. 3, one may deduce that the effect of exchange-correlations beyond the RPA consists in slight downward redistribution of the spectral weight, so that it partly compensating the changes caused by the LFE.

Scrutinizing the low-energy part of the bulk excitation spectra of Ti, we do not find any signature of an acoustic-like mode at small momentum transfers. This signals that the presence of several energy bands with a different Fermi velocity at the Fermi level does not lead automatically to the appearance of such a mode. Indeed, the condition of existence of at least two partly occupied energy bands with different Fermi velocities is necessary but not sufficient for the existence of such a mode. Instead, some weak features can be seen in the loss function in Fig. 2(c) in the energy region below 2 eV. However, they cannot be interpreted as plasmonic modes since the real part of dielectric function does not cross the zero axis at these energies. We interpret these peaks in the loss function as an enhanced number of incoherent electron-hole pairs. It is known that at large momentum transfers inclusion of the TD-LDA kernel may significantly increase the amplitude of the loss function at low energies as a result of excitonic effects [75]. In Fig. 4, we compare the dielectric function and the loss function for Ti calculated in the RPA and the TD-LDA at a large  $Q$  along the  $\langle 001 \rangle$  symmetry direction. Here, one can observe some increase in  $\epsilon_2$  and  $L$  upon inclusion of the TD-LDA kernel. Nevertheless, we consider that this increase is not sufficient to consider it as a signature of the exciton

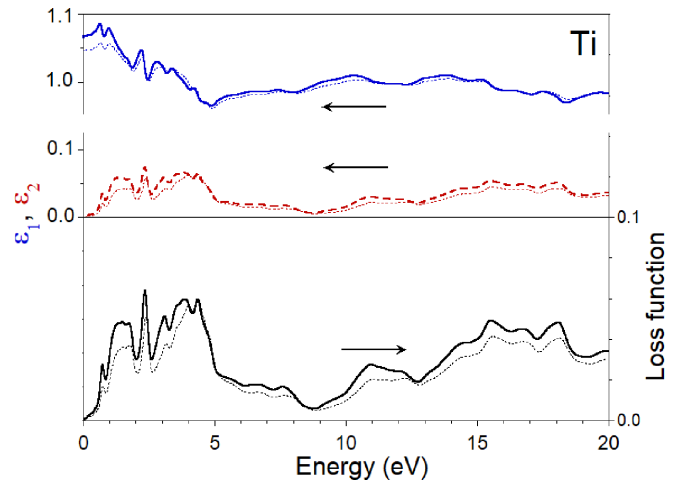


FIG. 4. Dielectric function  $\epsilon(\mathbf{Q}, \omega)$  and loss function  $L(\mathbf{Q}, \omega)$  in Ti calculated with inclusion of the LFE for the out-of-plane ( $Q = 2.11$  a.u.) polarizations. Black solid, blue solid, and red dashed thick lines show  $L$ ,  $\epsilon_1$ , and  $\epsilon_2$ , respectively, obtained in the TD-LDA framework. Dotted thin lines show the corresponding quantities calculated in the RPA.

formation in this material. The same holds for other symmetry directions in Ti and other materials under study. A possible explanation maybe relatively large valence density in all these materials, whereas such an exciton is expected in materials with significantly lower valence density [75].

Having the calculated bulk  $\epsilon(\omega)$ , we obtained the surface loss function  $\text{Im}[g]$  for a Ti surface. The corresponding curves are shown by green solid lines in Fig. 3. For the in-plane polarization, the surface loss function of Fig. 3(a) is dominated by a wide peak with energy of 12.4 eV corresponding to the surface plasmon  $\omega_{sp}$ . This value is close to the value of 12.2 eV obtained from the bulk plasmon energy  $\omega_p = 17.2$  eV using a classical expression  $\omega_{sp} = \omega_p/\sqrt{2}$ . However, the surface loss function in Ti significantly differs from the free-electron-gas (FEG) shape presenting additional strong peaks at 5.9 and 8.4 eV interpreted as surface modes. Even at an energy of 0.5 eV, there is a peak in the calculated  $\text{Im}[g]$ . However, its intensity is significantly smaller in comparison with the other surface modes.

The surface excitation spectra in the out-of-plane direction are even richer. The dominating peak in the surface loss function of Fig. 3(b), interpreted as a conventional surface plasmon, is observed at 12.5 eV. This value is about 0.5 eV higher than a classical value for a surface plasmon if we take  $\omega_p = 16.9$  eV for this direction. Other peaks at 5.9, 8.0, and 9.8 eV can be interpreted as surface plasmons as well. The surface loss function contains some other peaks with lower intensity. Among them, only the peak with energy of about 1.2 eV can be interpreted as a surface mode. However, its intensity is relatively low.

On the base of the calculated  $\epsilon(\omega)$ , we also evaluated the absorption spectrum  $\alpha(\omega)$  for small Ti particles. The corresponding data for both polarizations are presented in Fig. 3 by magenta solid lines. In the case of Fig. 3(a), we observe three main peaks in  $\alpha(\omega)$ . The peak with the largest absorption strength has an energy of 11.5 eV. Interestingly,

TABLE I. Positions of peaks in the calculated bulk and surface loss functions of Ti at a small momentum transfer in a hexagonal basal plane. The values in parentheses are obtained for polarization along the direction perpendicular to the basal plane. The plasmon energies of an isotropic FEG model are given for comparison. The experimental values were measured by the electron-energy-loss spectroscopy. The optical data of Ref. [73] are reported as well. All energies are in eV. The assignment of peaks given by the authors is reported as well. BP stands for “bulk plasmon,” SP for “surface plasmon,” and SS for “possible surface state.” In the *ab initio* calculation of Ref. [64], the energy scale is limited by 10 eV.

	This work	FEG [73]	[76]	[78]	[79]	[80]	[81]	[82]	[83]	[84]	[85]	[86]	[64] Calc.
BP 1	17.2 (16.9)	17.63	13.7	18.3 $3d \rightarrow 4sp$	17.5	17.0 BP+SP	15 BP	17.4 BP	17 BP	17.7 BP	17.3	18.0 BP	17.2
BP 2	– (10.1)			14.5 BP									
BP 3	8.7 (8.5)		7.0	9 $3d \rightarrow 4p$				8.6 $3d \rightarrow 4s$					9.59
BP 4	6.0 (6.0)		4.7	5 $3d \rightarrow 3d$	$\approx 5.5$								6.42
BP 5	0.5 (1.2)		0.45				$2d \rightarrow d$						
SP 1	12.4 (12.5)	12.47	10.7			11.5 BP	8 SP	$\approx 13$ SP	$\approx 13$ SP				
SP 2	– (9.8)												
SP 3	8.4 (8.0)		6.6						8.5 SS				
SP 4	5.9 (5.9)		4.2			5.0 SP							
SP 5	0.5 (1.2)		0.44										

$\epsilon_1$  has a local minimum of  $-1.5$  around this energy signaling that this mode is not a well-defined particle plasmon which is reflected in a rather wide loss peak. In contrast to what occurs with the surface plasmon energy, this energy value for the particle plasmon is significantly larger than a classical Mie plasmon value of 10.2 eV obtained from the FEG expression  $\omega_{Mp} = \omega_p/\sqrt{3}$ . The sharp loss peaks with energies of 5.7 and 8.1 eV are characterized by increasing strength in comparison with the bulk and surface cases. Analysis of  $\epsilon_1$  helps to interpret these features as particle plasmons. In the low-energy region of Fig. 3(a), we see in the magenta curve a plasmon peak at 0.5 eV with significantly lower intensity as it occurs in the bulk and at the surface.

Analyzing the particle absorption spectrum  $\alpha(\omega)$  of Fig. 3(b), we find three main peaks at 5.8, 7.8, and 11.5 eV. Again, the two lowest energy modes are clear particle plasmons, whereas the upper energy one is significantly damped. For this polarization, we find additional peaks in  $\alpha(\omega)$  at 6.5, 9.6, 14.0, and 15.6 eV with significantly lower intensity. They do not correspond to the collective electronic excitation in a Ti particle. In the low-energy region of Fig. 3(b), we detect in  $\alpha(\omega)$  two peaks at 0.4 and 1.2 eV. Since they are

rather wide and weak, the corresponding particle plasmons are strongly damped.

There are numerous experimental works devoted to the study of collective electronic excitations in titanium. The experimental data and our values for energy positions of the peaks in the loss function are summarized in Table I. In general, our plasmon energy of 17.2 (16.9) eV in the in-plane (out-of-plane) polarization is in a good agreement with the majority of values reported in the loss experiments. On the other hand, the most relevant feature of the experimental loss function measured in Ref. [76] is a double feature at 14.5 and 18.3 eV. A peak at 14.5 eV was assigned to the bulk plasmon according to the behavior of  $\epsilon_1$  at that energy, which shows a clear zero crossing and is accompanied with a small value of  $\epsilon_2$ . The value of 14.5 eV for the bulk plasmon energy reported in Ref. [76] seems to contradict our findings. A most intense experimental peak at 18.3 eV was then interpreted as due to  $3d \rightarrow 4sp$  interband transitions [77]. According to our findings, this experimental peak may correspond to the bulk plasmon in Ti. At lower energies, two oscillators were identified [76] at 5 and 9 eV, which were associated with  $3d \rightarrow 3d$  and  $3d \rightarrow 4p$  transitions [77]. On the other hand,

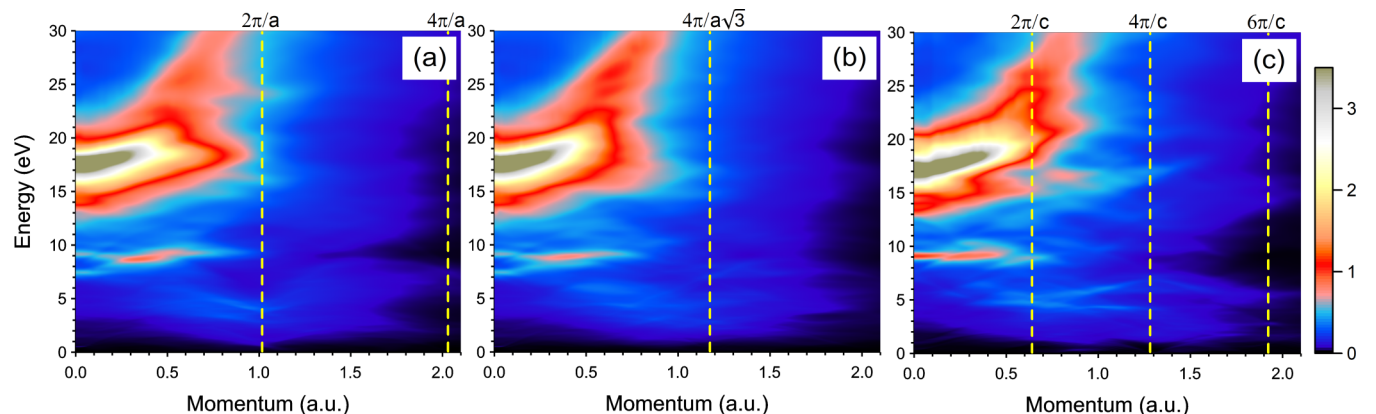


FIG. 5. Calculated loss function  $L(\mathbf{Q}, \omega)$  of Zr as a function of energy and momentum transfer  $\mathbf{Q}$  along  $\langle 100 \rangle$  (a),  $\langle 010 \rangle$  (b), and  $\langle 001 \rangle$  (c) symmetry directions of the h.c.p. lattice.

the value of 13.7 eV reported in Ref. [73] looks unreasonably low and is more close to the surface plasmon energy. The discrepancies reported in Table I may be related to problems with assignment of the measured loss peaks.

The experimental peaks at 8 [80], 8.6 [81], and 9 eV [76] correlate fairly well with the found here bulk plasmon at the energy of 8.7 (8.5) eV. On the other hand, our lower energy plasmon at 6.0 eV is in reasonable agreement with experimental peaks detected at 4.2 and 4.7 eV in Ref. [73] and 5 eV in Refs. [76,79]. The experimental features observed at 11.5 eV in Ref. [79], 13.7 eV in Ref. [73],  $\approx 13$  eV in Refs. [81,82], and 14.5 eV in Ref. [76] are rather close to our estimate for the surface plasmon energy.

The calculated loss function of Zr reported in Fig. 5 presents behavior qualitatively similar to that in titanium. The excitation spectrum at the in-plane momentum transfers in Figs. 5(a) and 5(b) is dominated by a strong plasmon peak at energy of 17.4 eV at small  $Q$ 's. This peak has positive dispersion and can be clearly resolved up to  $Q \sim 0.7$  a.u. At larger momentum transfers, this peak splits into two peaks characterized by different dispersions. The lower-energy peak is almost dispersionless and disappears at  $Q \sim 1.0$  a.u. The upper-energy peak possesses strong dispersion and reaches energy of above 30 eV at  $Q = 0.8$  a.u. along  $\langle 100 \rangle$  and at  $Q = 0.9$  a.u. along  $\langle 010 \rangle$ . At lower energies, we find in the in-plane loss function several other peaks. As seen in Fig. 6(a), there are three notable peaks at 7.4, 9.1, and 14.0 eV at small momentum transfers. Analyzing the behavior of the dielectric function reported in the same figure, we classify the 7.4 and 9.1 eV peaks as plasmons. On contrary, the 14.0 eV peak is not a collective excitation since  $\epsilon_1$  does not cross the zero line in the vicinity. Additionally, we find a weak peak in the loss function at 0.5 eV in close agreement with the optical data of Ref. [73], which can be interpreted as a plasmon. However, its intensity is almost negligible in comparison with other peaks. In the loss function of Figs. 5(a) and 5(b), one can see that the 7.4 and 9.1 eV plasmon peaks have positive and negative dispersion, respectively. Up to  $Q \sim 0.2$  a.u. they maintain similar strength. Beyond this  $Q$ , two curves meet each other and this results in the appearance of a much stronger single peak in the loss function with an energy of 8.5 eV. This peak has little positive dispersion and its presence in the loss function can be traced up to  $Q \sim 1.0$  a.u. along the  $\langle 100 \rangle$  direction and  $Q \sim 0.8$  a.u. along the  $\langle 010 \rangle$  one.

In case of the loss function calculated along the  $\langle 001 \rangle$  symmetry direction, we find essentially a similar behavior of the main plasmon peak. However, the anisotropy in the plasmon energy in Zr is larger in comparison with the Ti case. Thus, at small momentum transfers, the energy of plasmon in Zr is 16.9 eV. It has also strong positive dispersion. At finite momentum transfers some differences can be noted. Thus this mode splits into two peaks at  $Q \approx 0.2$  a.u. in this direction. The lower-energy peak again has a fairly flat dispersion and disappears at  $Q \sim 0.7$  a.u. The upper energy broad peak possessing strong positive dispersion can be seen up to  $Q \sim 0.7$  a.u. where it starts to split into several separate peaks. Similar to other directions, the upper energy peak reaches an energy of above 30 eV in this direction as well. Like in Ti, in Zr, we also find along the  $\langle 001 \rangle$  direction a notable second peak in the loss function even at small momentum transfers

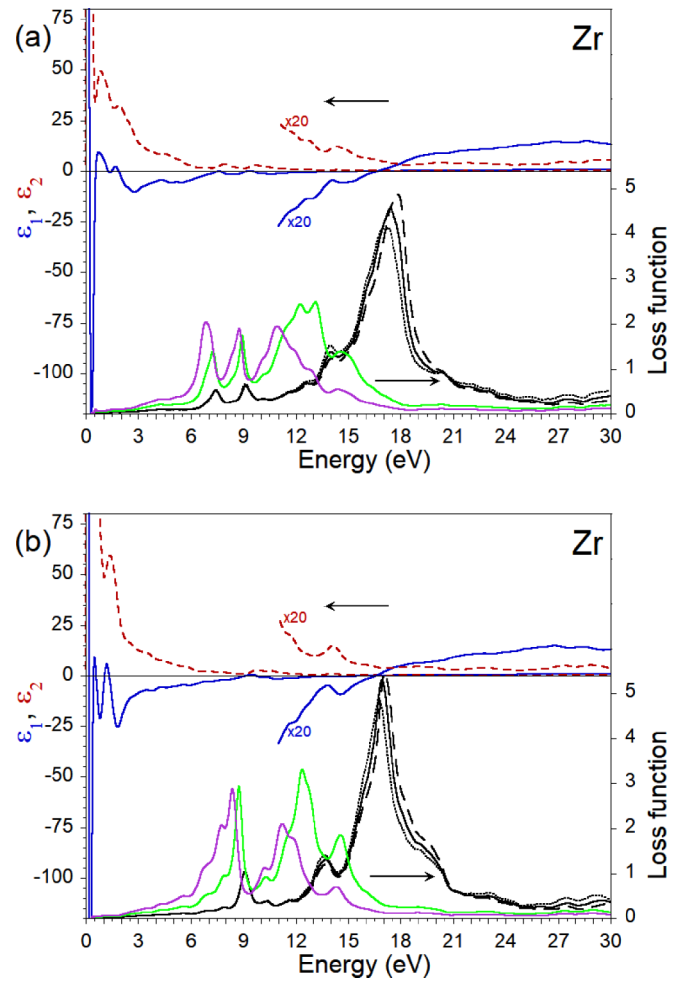


FIG. 6. Dielectric function  $\epsilon(\mathbf{Q}, \omega)$  and loss function  $L(\mathbf{Q}, \omega)$  in Zr calculated for (a) in-plane ( $Q = 0.008$  a.u.) and (b) out-of-plane ( $Q = 0.009$  a.u.) polarizations. Blue solid and red dashed lines show the real and imaginary parts of  $\epsilon$ , respectively. Black dotted lines show  $L$  calculated in the RPA and without inclusion of the LFE. Black long dashed lines represent  $L$  obtained in the RPA and the LFE included. Black, green, and magenta solid curves present bulk  $L(\omega)$ , surface  $\text{Im}[g(\omega)]$ , and particle  $\alpha(\omega)$ , respectively, evaluated in the TD-LDA framework with inclusion of the LFE.

at an energy of 9.1 eV. It maintains almost flat dispersion in the  $0 < Q < 0.5$  a.u. momentum range. As seen in Fig. 6(b), the loss function for small  $Q$  along the  $\langle 001 \rangle$  direction has a notable peak at an energy of 13.7 eV. It is difficult to classify it as a separate plasmon peak since  $\epsilon_1$  does not reach zero in the nearby energy region. However, one can note that the intensity of this peak for  $Q$  along  $\langle 001 \rangle$  is significantly larger in comparison to what occurs with a similar peak for the in-plane  $Q$  of Fig. 6(a).

Like in Ti, we do not observe any acoustic-like mode in the low-energy region of the excitation spectrum of Zr. In Fig. 5, one can only find some weak peaks at energies below 1 eV at finite momentum transfers in the  $\langle 001 \rangle$  direction. Similar to the Ti case, we interpret these features as electron-hole pairs.

Comparison of our calculated values of the main 17.4 (16.9) eV plasmon in Zr with available experimental data reveals some systematic deviation as seen in Table II. In

TABLE II. Positions of peaks in the calculated bulk and surface loss functions of Zr at a small momentum transfer in a hexagonal basal plane. The values in parentheses are obtained for polarization along the direction perpendicular to the basal plane. The plasmon energies of an isotropic FEG model are given for comparison. The experimental values were measured by the electron-energy-loss spectroscopy. The optical data of Refs. [27,73] are reported as well. All energies are in eV. The assignment of peaks given by the authors is reported as well. BP stands for “bulk plasmon,” SP for “surface plasmon,” and SLE for “surface localized excitation.”

	This work	FEG	[27]	[73]	[77]	[84]	[87]	[88]	[89]	[90]	[91]	[92]	[93]
BP 1	17.4 (16.9)	15.39	17.78	14.6	16.3	16.9	17.0 BP	16.8	16.2	16.3	16.1	16.6	15.6
BP 2	14.0 (13.7)												
BP 3	9.1 (9.1)		10.29	5.7	8.5 $4d \rightarrow 5p$	$\sim 8$	7.4 BP			8.5 $4d,5s \rightarrow 5p$	8.6		8.0
BP 4	7.4 (—)		3.88		4.3 $4d \rightarrow 4d$	$\sim 8$			4.2	3.0 $4d \rightarrow 4d$			
BP 5	0.5 (1.1)		1.54	0.5									
SP 1	12.5 (12.4)	10.88		13.4			13.3 SP		11.8 SP	13.2 SP			
SP 2	9.0 (8.7)												
SP 3	7.2 (—)			5.2			3.5 SP		7.6 SLE				
SP 4	0.5 (1.1)			0.5									

general, our calculated values are larger than the measured ones. Only the measured values of 17 eV of Ref. [87], 16.9 eV of Ref. [84], and 16.8 eV of Ref. [88] are close to our data. On the other hand, several measurements [77,89–92] reported values in the 16.1–16.6 eV interval. In Refs. [73,93], even lower values for the plasmon energy in Zr were reported. Indeed, such spread in the experimental values is difficult to understand. Probably it depends on the experimental conditions. Actually, we expect that the calculated plasmon values should be somewhat lower than the ones obtained here. A reason for that is a possible impact of the Zr semicore  $4s$  electronic states located at about 27 eV below the Fermi level [47], which were not included in the present calculations. We expect that inclusion of these semicore states would shift down the calculated plasmon energy value like it was found in the case of lead [94]. However, a downward shift of the plasmon peak energy in Zr caused by the interband transitions involving these semicore states should not be as significant as in the case of Pb and to be limited to few tenths of eV.

Like it was done for Ti, we evaluated for zirconium the surface loss function and particle absorption spectrum presented in Fig. 6 by green and magenta solid lines, respectively. At the surface, the excitation spectrum in the in-plane direction of Fig. 6(a) is dominated by a double-peak broad structure centered at 12.5 eV. This value correlates rather well with the classical value of 12.3 eV for the surface plasmon if we take as reference the calculated bulk plasmon energy of 17.4 eV. On the other hand, the FEG surface plasmon energy of 10.88 eV deviates substantially from it. Moreover, the FEG simple picture about surface plasmon breaks completely in Zr since we present three other plasmon peaks in the in-plane surface loss function at 0.5, 7.2, and 9.0 eV. If we take the calculated values for the corresponding bulk plasmons in Table II, we obtain for the surface plasmon energies of 0.35, 6.4, and 9.9 eV which deviate notably from the calculated ones. This is related to the strong deviation of the dielectric function in this energy range from a Drude-like behavior. Note that a peak observed in the surface loss function at energies about 14.5 eV in Fig. 6(a) can not be interpreted as a surface plasmon since  $\epsilon_1$  does not approach  $-1$  in the nearby region.

If we take a bulk dielectric function for the out-of-plane direction, Fig. 6(b), the resulting surface loss function shows

two clear surface plasmon peaks at 8.7 and 12.4 eV. These values only slightly differ from those in the in-plane direction despite strong differences in the surface loss functions in both these polarizations. Another surface plasmon peak can be discerned in the out-of-plane loss function at 1.1 eV with negligible spectral weight. Like in the case of Fig. 6(a) in the out-of-plane surface loss function of Fig. 6(b), there is a notable peak at 14.5 eV, which can be interpreted as a severely dumped collective surface excitation based on analysis of the real part of dielectric function.

Figure 6 presents also the particle absorption spectra calculated by using the bulk dielectric function of Zr. For  $\alpha(\omega)$  with in-plane polarization of Fig. 6(a), we observe three well defined particle plasmon peaks at 6.9, 8.7, and 11.0 eV. One more plasmon peak with low spectral weight can be detected at 1.1 eV. A weak broad peak at 14.5 eV cannot be interpreted as a well-defined collective excitation of a Zr particle. In the case of out-of-plane polarization, the resulting  $\alpha(\omega)$  presented in Fig. 6(b) possesses two dominating peaks with energies of 8.4 and 11.2 eV, which can be interpreted as particle plasmons. In the case of the peak seen in  $\alpha(\omega)$  at 14.4 eV, the real part of the dielectric function is too far from fulfilling the  $\epsilon_1 = -2$  condition.

## B. $\text{TiH}_2$ and $\text{ZrH}_2$

### 1. Band structure

The energy bands of  $\text{TiH}_2$  and  $\text{ZrH}_2$  are reported in Fig. 7. From comparison with the electronic structure of pure Ti and Zr in Fig. 1, one can see strong variation in the energy bands induced by hydrogen absorption. Detailed analysis of partial composition of electronic bands in these hydrides can be found in Refs. [13–15,18,47,95,96]. In the hydrides, the lowest energy band is formed by metal-H bonding states. Next, four bands correspond to the metal  $d$  states. In  $\text{TiH}_2$ , the band located at the  $\Gamma$  point at the energy of 1.0 eV corresponds to the antibonding combination of the H states. A similar band in the case of  $\text{ZrH}_2$  is observed at  $\Gamma$  at the energy of  $-0.3$  eV. Like in the pure Ti and Zr metals, in their hydrides, we observe several energy bands crossing the Fermi level with distinct Fermi velocities. For this reason, we performed detailed analysis

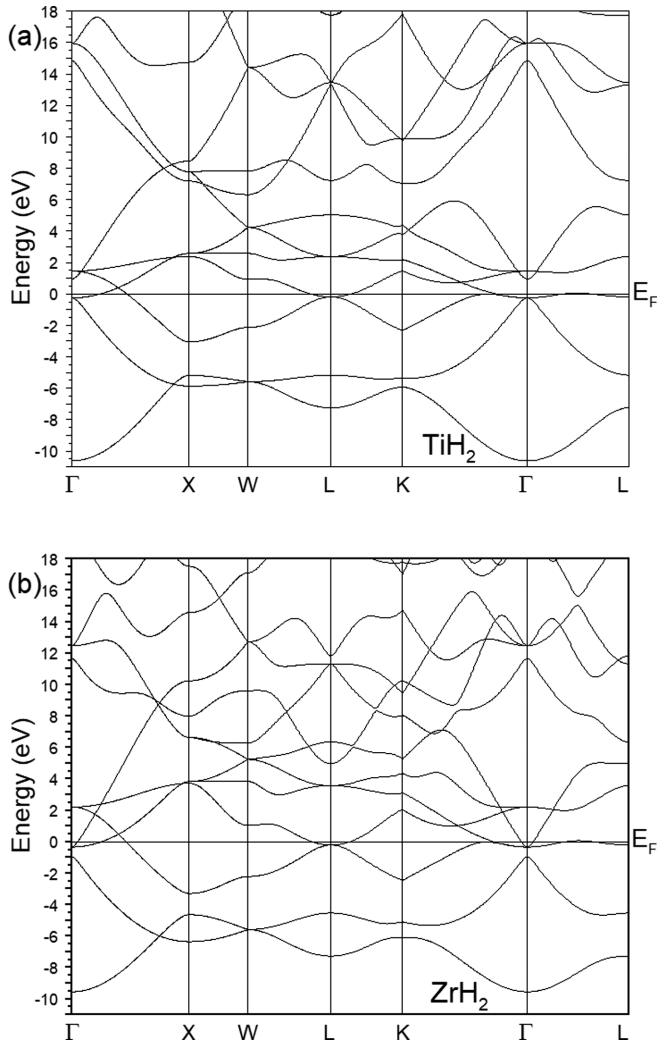


FIG. 7. Calculated  $\text{TiH}_2$  (a) and  $\text{ZrH}_2$  (b) band structure along some symmetry directions in the Brillouin zone. The energy is relative to the Fermi level  $E_F$  set to zero.

of the low-energy excitation spectra in an attempt to find an acoustic-like plasmon.

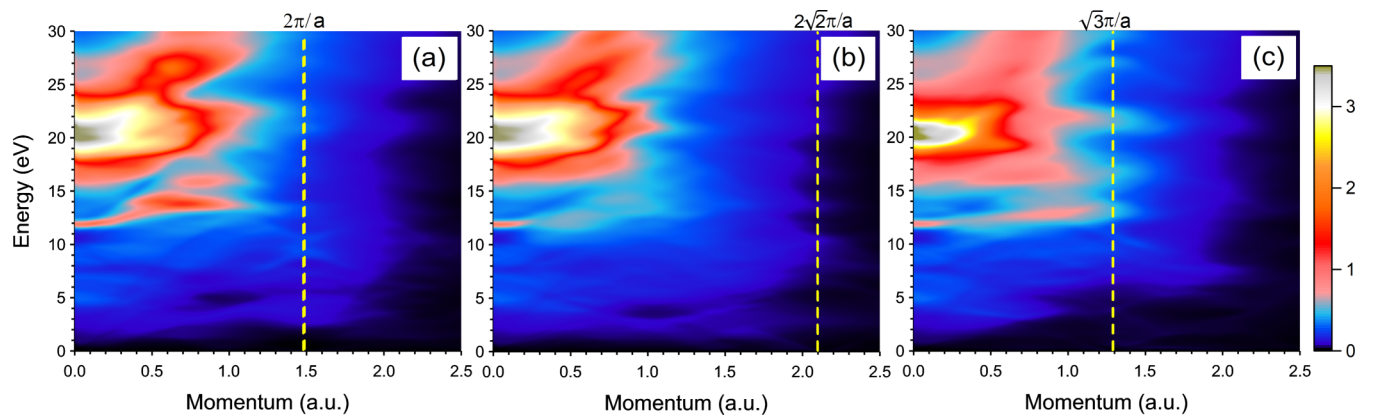


FIG. 8. Calculated loss function  $L(\mathbf{Q}, \omega)$  of  $\text{TiH}_2$  as a function of energy and momentum transfer  $\mathbf{Q}$  along  $\langle 100 \rangle$  (a),  $\langle 110 \rangle$  (b), and  $\langle 111 \rangle$  (c) symmetry directions of the f.c.c. lattice.

## 2. Loss function

The calculated loss function of  $\text{TiH}_2$  is reported in Fig. 8. Like in the previous systems, the loss function is calculated along the main three symmetry directions. However, since the  $\text{TiH}_2$  lattice is the f.c.c. one, these symmetry directions are defined according to the respective BZ. Comparing different panels in Fig. 8, one can observe that the excitation spectrum in  $\text{TiH}_2$  is dominated by a wide double-peak structure in the 15–25 eV energy range. The energy positions of two peaks are 20 and 21 eV at small momentum transfers in all three directions. The plasmon energy in  $\text{TiH}_2$  is significantly larger in comparison with that in pure Ti. This is in stark contrast with the case of Pd where absorption of hydrogen results in significant reduction of the plasmon energy [97]. We explain such phenomenon by the increasing averaged valence electronic density in  $\text{TiH}_2$ . As follows from Tables I and III, the variation of plasmon energies in both systems is fairly well described by a simple FEG model by using the average valence electron densities. Nevertheless, our average value of 20.5 eV for these two modes in Ti notably deviates from the FEG value of 19.35 eV.

Initial dispersion of the 20 and 21 eV peaks is almost flat up to  $q \sim 0.25$  a.u. At larger momentum transfers, its dispersion turns to be positive. Along the  $\langle 100 \rangle$  direction of Fig. 8(a), these peaks merge at large momentum transfers and are characterized by rather small positive dispersion. The respective broad feature can be detected up to  $Q \sim 1.2$  eV. Additionally, at  $Q \sim 0.5$  a.u., we observe emergence of a second broad peak at larger energy. This peak possesses strong upward dispersion and reaches energy of 30 eV at  $Q$  about 1.0 a.u. Similar behavior of this feature in the loss function is observed along the  $\langle 110 \rangle$  direction. Only small quantitative changes in the calculated loss function between these two symmetry directions at energies above 17 eV can be found. Essentially, the same behavior in the high-energy range is observed in the loss function for the  $\langle 111 \rangle$  direction as well. The only changes are related to the relative strength of both dominated peaks at finite momentum transfers and some other tiny features.

A notable anisotropy in the loss function can be found at energies below  $\sim 17$  eV. Thus, in Fig. 8, one can see a narrow peak with an energy of 11.9 eV at small momentum

TABLE III. Positions of peaks in the calculated bulk and surface loss functions of TiH<sub>2</sub> at small momentum transfer. The values measured in the electron energy-loss spectroscopy experiments are given for comparison. All energies are in eV. SP stands for “surface plasmon.”

	This work	FEG	[76]	[81]	[83]	[86]	[98]	[64] Calc.
BP 1	20+21	19.35	19	17	20.7 ± 0.3	20.8	20.2	16.5
BP 2	11.9							
BP 3	8.6			≈ 8				
BP 4	5.0			5 H1s+Ti3d → Ti3d				
SP 1	17.2							
SP 2	15.5	13.68		≈ 15	14 SP?			
SP 3	11.6							
SP 4	4.6							

transfers. Along  $\langle 100 \rangle$  up to  $Q \sim 0.5$  a.u., this peak has a parabolic-like positive dispersion. At an energy of 13.5 eV, it merges into the broader peak characterized by a flat dispersion in the  $0.3 < Q < 1.0$  a.u. momentum range. Along the  $\langle 110 \rangle$  direction in the loss function, a similar peak is observed at small momentum transfers. However, along  $\langle 110 \rangle$ , this mode exists only at momentum transfers smaller than 0.3 a.u. Such a mode also appears in the  $\langle 111 \rangle$  direction. At  $Q = 0$ , it has the same energy and positive dispersion with essentially the same spectral weight up to  $Q \sim 0.25$  a.u. Beyond this momentum transfer, this peak still can be resolved in the loss function up to an energy of 13 eV but with a significantly reduced spectral weight. Upon increasing momentum transfer, this feature becomes more robust and can be clearly resolved in the  $\sim 0.6 < Q < \sim 1.2$  a.u. interval.

The calculated values of the bulk plasmon energies in TiH<sub>2</sub> are compared in Table III with the values reported in other publications. Our data deviate substantially from the value of 16.5 eV calculated in Ref. [64]. On the other hand, in the table, one can see some spread in the experimental data with a plasmon energy varying from 17 eV in Ref. [81] to 20.8 eV of [86]. Our average plasmon energy of 20.5 eV is closer to 20.2 eV found in Ref. [98] and  $20.7 \pm 0.3$  eV measured in Ref. [83]. Probably, the lower values obtained in other measurements are related to the different content of hydrogen in the samples.

In Fig. 9, we report the dielectric and loss functions of TiH<sub>2</sub> evaluated at small  $Q$ . In the calculated loss function, in addition to the plasmon peaks discussed above, we observe several other broad features. In the loss function, there are peaks with energies of 5.0, 7.0, 8.6, 9.3, 11.9, and 27 eV. Inspecting the behavior of the dielectric function, we interpret three peaks with energies of 5.0, 8.6, and 11.9 eV as bulk collective excitations. As follows from Table III, probably in the experiments of Refs. [81,83] some related features were detected.

From Fig. 9, one can deduce that the LFE produce an effect on the excitation spectrum in TiH<sub>2</sub> similar to that in Ti and Zr. The same can be said regarding the exchange-correlation effects beyond the RPA.

Despite the presence of several energy bands in TiH<sub>2</sub> at the Fermi level, we do not find any acoustic-like mode in this material as it occurs in Ti and Zr. Like in those materials, in the loss function of TiH<sub>2</sub> we do not observe any notable features in the low-energy range at all momentum transfers. Only some

small features in the loss function of TiH<sub>2</sub> related to the electron-hole pairs can be discerned in the low-energy interval. Moreover, we do not see any difference in the excitation spectra of TiH<sub>2</sub> and ZrH<sub>2</sub> related to the different positions of the antibonding H band according to the Fermi level. This might be related to the small occupied part of this band in ZrH<sub>2</sub> resulting in small weight of the corresponding intraband transitions.

In Fig. 9, we plot also the surface loss function in TiH<sub>2</sub> obtained on the basis of the calculated  $\epsilon(\omega)$ . The evaluated  $\text{Im}[g(\omega)]$  presents several peaks which can be interpreted as surface collective excitations. The dominating feature consists of two peaks with energies of 15.5 and 17.2 eV. These values deviate significantly from the predictions of the FEG model. Moreover, if we use the classical model for an estimation of the surface plasmon energy, the bulk plasmon values of 20 and 21 eV calculated here are in notable discrepancy as well (14.1 and 14.9 eV). It reflects a notable deviation of the calculated dielectric function in TiH<sub>2</sub> from the simple FEG behavior caused by numerous interband transitions. Additionally, the surface loss function presents a sharp peak at 11.6 eV with

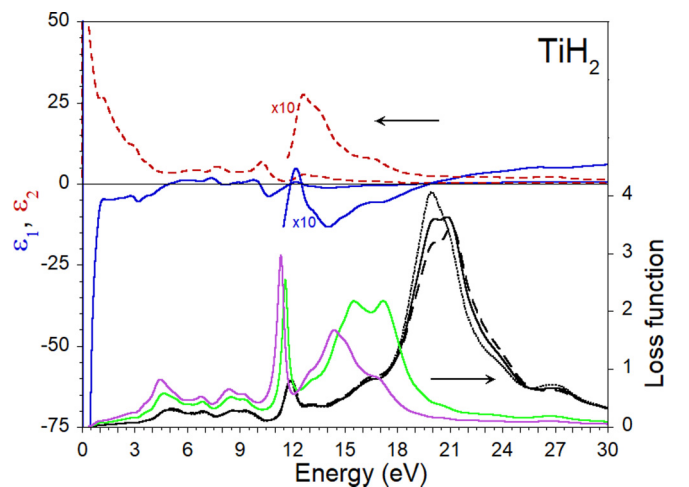


FIG. 9. Dielectric function  $\epsilon(\mathbf{Q}, \omega)$  and loss function  $L(\mathbf{Q}, \omega)$  in TiH<sub>2</sub> calculated at  $Q = 0.010$  a.u. Blue solid and red dashed lines show the real and imaginary parts of  $\epsilon$ , respectively. Black dotted line shows  $L$  calculated in the RPA and without inclusion of the LFE. Black long dashed line represents  $L$  obtained in the RPA and the LFE included. Black, green, and magenta solid curves present bulk  $L(\omega)$ , surface  $\text{Im}[g(\omega)]$ , and particle  $\alpha(\omega)$ , respectively, evaluated in the TD-LDA framework with inclusion of the LFE.

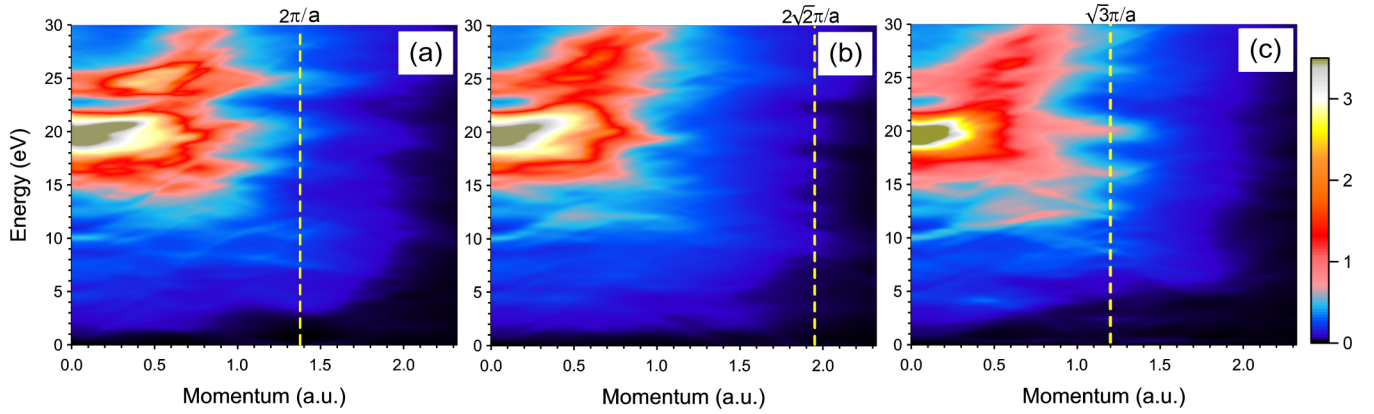


FIG. 10. Calculated loss function  $L(\mathbf{Q}, \omega)$  of  $\text{ZrH}_2$  as a function of energy and momentum transfer  $\mathbf{Q}$  along  $\langle 100 \rangle$  (a),  $\langle 0110 \rangle$  (b), and  $\langle 111 \rangle$  (c) symmetry directions of the f.c.c. lattice.

notable spectral weight. In terms of predicting this feature, the FEG model breaks completely since  $\epsilon_1$  varies very strongly in this energy region. At lower energies, we detect several other peaks in the surface loss function. Among them, only a feature with an energy of 4.6 eV may be interpreted as a surface collective excitation since the condition  $\epsilon_1 = -1$  is fulfilled in this energy region.

Regarding the  $\text{TiH}_2$  particle absorption spectrum  $\alpha(\omega)$  presented in Fig. 9, we observe several peaks as well. On the large energy side, a dominating peak is located at the energy of 14.4 eV although its spectral weight is significantly reduced in comparison with the bulk and surface cases. A very prominent plasmon peak in  $\alpha(\omega)$  is located at 11.3 eV. Among all the collective excitations in  $\text{TiH}_2$ , this possesses the longest lifetime since the peak is the narrowest one. At lower energies, we observe several other peaks in the particle excitation spectra. Analysis of the  $\epsilon_1$  behavior helps to determine the 4.5 eV feature as a collective excitation whereas the others correspond to just electron-hole pairs.

The calculated loss function for  $\text{ZrH}_2$  is reported in Fig. 10 where one can see that the excitation spectrum in this material is dominated by a plasmon peak with an energy of 19.4 eV at small momentum transfers in all symmetry directions. The main plasmon peak is wide due to efficient decay into electron-hole pairs. Like in other studied systems, this peak in  $\text{ZrH}_2$  also has a positive dispersion and can be observed up to momentum transfer reaching  $\sim 1$  a.u. in all directions. At larger momentum transfers, its presence hardly can be detected. Instead, several weak peaks exist there, which are related to incoherent electron-hole excitations. Our calculated plasmon value of 19.4 eV in  $\text{ZrH}_2$  is only slightly lower than in  $\text{TiH}_2$ , which is in contrast to the significantly lower plasmon value derived in the FEG model determined by the average valence density in this compound. On the other hand, as seen in Table IV, we find rather good agreement between our calculated value of the plasmon energy in  $\text{ZrH}_2$  with the 19 and 19.6 eV values measured experimentally [88,92].

In contrast to  $\text{TiH}_2$ , in the loss function of  $\text{ZrH}_2$ , we observe additional appreciable features at larger energies. As seen in Figs. 10 and 11, at small momentum transfers, two peaks are located at the energies of 23.7 and 25.5 eV. Analysis of behavior of  $\epsilon$  in the nearby energy region confirms that these features

do not correspond to any collective excitations. Moreover, its intensity is significantly lower than that of the main plasmon, which can explain why it was not detected experimentally. Also, its intensity or even existence might be influenced by incorporation in the calculations of the semicore electronic states of Zr. Another difference consists in the small spectral weight of the low-energy plasmon with energy of 10 eV at small momentum transfers. This peak is rather well resolved in the loss function of Fig. 11 and we interpret it as a collective excitation. However, it can be barely seen in the excitation spectra of Fig. 10 in all three symmetry directions. Indeed, many other rather broad and weak peaks can be detected in the calculated loss function of  $\text{ZrH}_2$ . As seen in Fig. 11, in some cases, its existence correlates with the zero-crossings in  $\epsilon_1$  at close energies. Among these peaks, we may unambiguously interpret as collective excitation the 4.7-eV peak. The nature of the others is questionable.

Like in the previously studied systems, we investigated the impact of LFE and dynamical exchange-correlations on the excitation spectrum in  $\text{ZrH}_2$ . From Fig. 11, it is clear that both ingredients work in a similar fashion in this compound as well.

We calculated the surface loss function in  $\text{ZrH}_2$ , which is represented by the green solid line in Fig. 11. In it, we observe the dominating feature consisting of two peaks with energies of 14.5 and 15.7 eV. Again, the number and energy positions of

TABLE IV. Positions of peaks in the calculated bulk and surface loss functions of  $\text{ZrH}_2$  at small momentum transfer. The bulk plasmon energies measured in the electron energy-loss spectroscopy experiments are given for comparison. All energies are in eV.

	This work	FEG	[88]	[92]
BP 1	19.4	17.29	19.6	19
BP 2	10.1			
BP 3	4.7			
SP 1	15.7			
SP 2	14.5			
SP 3	12.1	12.23		
SP 4	9.9			
SP 5	4.6			

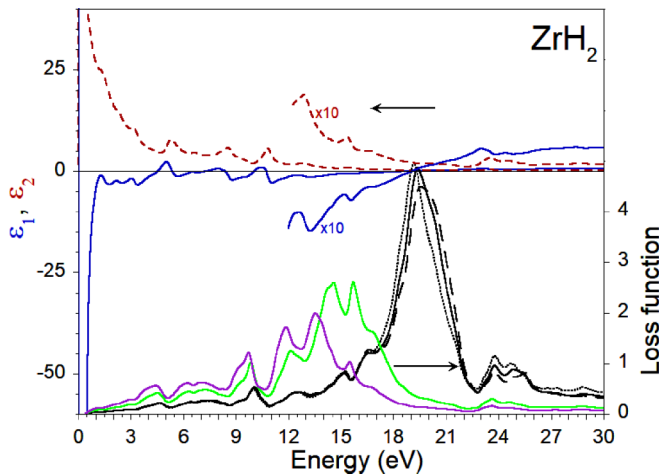


FIG. 11. Dielectric function  $\epsilon(\mathbf{Q}, \omega)$  and loss function  $L(\mathbf{Q}, \omega)$  in  $\text{ZrH}_2$  calculated at  $Q = 0.010$  a.u. Blue solid and red dashed lines show the real and imaginary parts of  $\epsilon$ , respectively. Black dotted line shows  $L$  calculated in the RPA and without inclusion of the LFE. Black long dashed line represents  $L$  obtained in the RPA and the LFE included. Black, green, and magenta solid curves present bulk  $L(\omega)$ , surface  $\text{Im}[g(\omega)]$ , and particle  $\alpha(\omega)$ , respectively, evaluated in the TD-LDA framework with inclusion of the LFE.

these surface collective excitations contradict the FEG model. Like in bulk, the surface loss function presents several other peaks. Among them, we interpret the peaks with energies of 4.6, 9.9, and 12.1 eV as surface collective excitations.

In the calculated  $\text{ZrH}_2$  particle absorption spectrum, depicted in Fig. 11 by magenta solid line, we observe several peaks. Analysis of  $\epsilon$  helps us to interpret the 4.4, 9.7, and 11.9 eV peaks as particle plasmons. Interestingly, it is difficult to interpret formally as collective excitation the most prominent peak at the energy of 13.6 eV in the absorption spectrum since  $\epsilon_1$  reaches only  $-1.5$  in the corresponding energy interval. Nevertheless, we consider that it can be classified as a collective excitation taking a softer definition.

#### IV. CONCLUSIONS

In conclusion, we studied the collective electronic excitations in Ti and Zr metals in the framework of time-dependent density-functional theory. Strong plasmon peaks with energy of 17.2 (16.9) and 17.4 (16.9) eV at small momentum transfers

for the in-plane (out-of-plane) polarization are found in Ti and Zr, respectively. The plasmons have positive dispersion and can be traced up to an energy exceeding 30 eV. At lower energy, we find several other plasmon modes with significantly lower spectral weight. They are realized at different energies and possess a positive dispersion.

Similar calculations were performed for the stoichiometric dihydrides of these metals,  $\text{TiH}_2$  and  $\text{ZrH}_2$ . We find that the plasmon energies in these materials are significantly larger in comparison to pure metals. Thus the main plasmon energy in  $\text{TiH}_2$  reaches an average value of 20.5 eV at small momentum transfers whereas in  $\text{ZrH}_2$  it blueshifts up to 19.4 eV. A second plasmon mode with energy of 10 eV is very weak in this material. Instead, we find another peak in the loss function at an energy of 24.5 eV. The calculated values for the plasmon energies in all the materials considered in this work are in pretty good agreement with existing experimental data.

Like it occurs in pristine metals, we do not find any collective excitations in their hydrides at low energies. Thus, despite the presence of several energy bands crossing the Fermi level with different Fermi velocities, we do not find any acoustic-like mode in all the studied systems.

On the basis of the calculated bulk dielectric functions, we investigated the excitation spectra at a surface and in a small particle of these materials. The data obtained reveal rich plasmonic structures in such systems. In particular, several plasmonic excitations can be realized. Comparison of the particle absorption spectra in the Ti and Zr with those in their hydrides reveals strong variation in the absorption spectra upon the hydrogen uptake. It may be relevant for the ultraviolet plasmonics [99] employing these materials.

#### ACKNOWLEDGMENTS

The research was funded by the Tomsk Polytechnic University Competitiveness Enhancement Program. I.V.S. acknowledges financial support from the Ministry of Education and Science of the Russian Federation within the governmental program Megagrants (State Task No. 3.9003.2017/П220 or 3.9003.2017/9.10). V.M.S. and E.V.C. acknowledge the partial support from the University of the Basque Country UPV/EHU, Grant No. IT-756-13 and the Spanish Ministry of Economy, Industry and Competitiveness MINEICO, Project Nos. FIS2016-76617-P and FIS2016-75862-P. V.M.S. acknowledges project PI2017-30 of the Departamento de Educación, Política Lingüística y Cultura of the Basque government.

[1] T. Graham, Proc. Royal Soc. **18**, 212 (1869).  
 [2] W. M. Müller, J. P. Blackledge, and G. G. Libowitz (Eds.) *Metal Hydrides* (Academic, New York, 1968).  
 [3] *Hydrogen in Metals I*, edited by G. Alefeld and J. Völkl, Topics in Applied Physics Vol. 28 (Springer-Verlag, Berlin, 1978).  
 [4] *Hydrogen in Metals II*, edited by G. Alefeld and J. Völkl, Topics in Applied Physics Vol. 29 (Springer-Verlag, Berlin, 1978).  
 [5] M. V. C. Sastri, *Metal Hydrides: Fundamentals and Applications* (Springer-Verlag, Berlin, 1998).

[6] Y. Fukai, *The Metal-Hydrogen System* (Springer-Verlag, Berlin, 1993).  
 [7] M. P. Puls, *The Effect of Hydrogen and Hydrides on the Integrity of Zirconium Alloy Components* (Springer-Verlag, London, 2012).  
 [8] J. H. Weaver, D. J. Peterman, D. T. Peterson, and A. Franciosi, *Phys. Rev. B* **23**, 1692 (1981).  
 [9] A. San-Martin and F. D. Manchester, *Bull. Alloy Phase Diagrams* **8**, 30 (1987).

- [10] E. Zuzek, J. P. Abriata, A. San-Martin, and F. D. Manchester, *Bull. Alloy Phase Diagrams* **11**, 385 (1990).
- [11] P. A. Schulz and C. S. Snow, *Modelling Simul. Mater. Sci. Eng.* **24**, 035005 (2016).
- [12] A. C. Switendick, *J. Less-Common Met.* **101**, 191 (1984).
- [13] W. Wolf and P. Herzig, *J. Phys.: Condens. Matter* **12**, 4535 (2000).
- [14] R. Quijano, R. de Coss, and D. J. Singh, *Phys. Rev. B* **80**, 184103 (2009).
- [15] S. E. Kulkova, O. N. Muryzhnikova, and I. I. Naumov, *Phys. Solid State* **41**, 1763 (1999).
- [16] K. V. Shanavas, L. Lindsay, and D. S. Parker, *Sci. Rep.* **6**, 28102 (2016).
- [17] Q. Xu and A. Van der Ven, *Phys. Rev. B* **76**, 064207 (2007).
- [18] S. Er, M. J. van Setten, G. A. de Wijs, and G. Brocks, *J. Phys.: Condens. Matter* **22**, 074208 (2010).
- [19] R. Weiyi, X. Pingchuan, and S. Weigu, *Physica B (Amsterdam)* **405**, 2057 (2010).
- [20] P. Zhang, B. Wang, C. He, and P. Zhang, *J. Comp. Mat. Sci.* **50**, 3297 (2011).
- [21] F. Wang and H. R. Gong, *Int. J. Hydrogen Energy* **37**, 9688 (2012).
- [22] S. Yamanaka, K. Yamada, K. Kurosaki, M. Uno, K. Takeda, H. Anada, T. Matsuda, and S. Kobayashi, *J. Alloys. Comp.* **330-332**, 99 (2002).
- [23] S. Nakao, K. Saitoh, T. Hirahara, M. Ikeyama, M. Tazawa, P. Jin, H. Niwa, S. Tanemura, Y. Miyagawa, S. Lmiyagawa, and K. Yasuda, *Thin Solid Films* **343-344**, 195 (1999).
- [24] D. W. Lynch and W. R. Hunter, in *Handbook of Optical Constants of Solids III*, edited by E. D. Palik (Elsevier, Amsterdam, 1997), p. 233.
- [25] S. Adachi, *The Handbook on Optical Constants of Metals* (World Scientific, Singapore, 2012).
- [26] S. Krishnan, C. D. Anderson, and P. C. Nordine, *Phys. Rev. B* **49**, 3161 (1994).
- [27] D. E. Azofeifa, N. Clark, W. E. Vargas, H. Solis, E. Avendano, M. Cambrono, and D. Valverde-Mendez, *Int. J. Hydrogen Energy* **42**, 22373 (2017).
- [28] D. Pines, *Can. J. Phys.* **34**, 1379 (1956).
- [29] D. Pines and P. Nozières, *The Theory of Quantum Liquids: Normal Fermi Liquids* (W. A. Benjamin, New York, 1966), Vol. 1.
- [30] E. Runge and E. K. U. Gross, *Phys. Rev. Lett.* **52**, 997 (1984).
- [31] E. K. U. Gross and W. Kohn, *Phys. Rev. Lett.* **55**, 2850 (1985).
- [32] B. N. J. Persson and E. Zaremba, *Phys. Rev. B* **31**, 1863 (1985).
- [33] A. Liebsch, *Electronic Excitations at Metal Surfaces* (Plenum, New York, 1997).
- [34] R. H. Ritchie, *Phys. Rev.* **106**, 874 (1957).
- [35] S. A. Maier, *Plasmonics: Fundamentals and Applications* (Springer, New York, 2007).
- [36] V. M. Silkin, E. V. Chulkov, I. Y. Sklyadneva, and V. E. Panin, *Sov. Phys. J.* **27**, 762 (1984).
- [37] G. B. Bachelet, D. R. Hamann, and M. Schlüter, *Phys. Rev. B* **26**, 4199 (1982).
- [38] D. M. Ceperley and B. J. Alder, *Phys. Rev. Lett.* **45**, 566 (1980); as parametrized by J. P. Perdew and A. Zunger, *Phys. Rev. B* **23**, 5048 (1981).
- [39] D. Errandonea, Y. Meng, M. Somayazulu, and D. Hausermann, *Physica B (Amsterdam)* **355**, 116 (2005).
- [40] B. Olinger and J. C. Jamieson, *High Temp. High Pressures* **5**, 123 (1973).
- [41] M. Magnuson, L. Tengdelius, G. Greczynski, L. Hultman, and H. Högberg, *Thin Solid Films* **649**, 89 (2018).
- [42] S. S. Sidhu, N. S. S. Murthy, F. P. Campos, and D. D. Zaubers, *Adv. Chem. Ser.* **39**, 87 (1963).
- [43] H. L. Yakel Jr., *Acta Crystallogr.* **11**, 46 (1958).
- [44] D. Setoyama, J. Matsunaga, H. Muta, M. Uno, and S. Yamanaka, *J. Alloys Compd.* **381**, 215 (2004).
- [45] P. Villars, L. D. Calvert, and W. B. Pearson, *Person's Handbook of Crystallographic Data for Intermetallic Phases* (Materials Park, OH: ASM International, 1991).
- [46] J. S. Cantrell, R. C. Bowman, Jr., and D. B. Sullenger, *J. Phys. Chem.* **88**, 918 (1984).
- [47] M. Magnuson, S. Schmidt, L. Hultman, and H. Högberg, *Phys. Rev. B* **96**, 195103 (2017).
- [48] V. M. Silkin, E. V. Chulkov, and P. M. Echenique, *Phys. Rev. B* **68**, 205106 (2003).
- [49] S. L. Adler, *Phys. Rev.* **126**, 413 (1962).
- [50] N. Wiser, *Phys. Rev.* **129**, 62 (1963).
- [51] Y. Q. Cai, P. C. Chow, O. D. Restrepo, Y. Takano, K. Togano, H. Kito, H. Ishii, C. C. Chen, K. S. Liang, C. T. Chen, S. Tsuda, S. Shin, C. C. Kao, W. Ku, and A. G. Eguiluz, *Phys. Rev. Lett.* **97**, 176402 (2006).
- [52] R. Hambach, C. Giorgetti, N. Hiraoka, Y. Q. Cai, F. Sottile, A. G. Marinopoulos, F. Bechstedt, and L. Reining, *Phys. Rev. Lett.* **101**, 266406 (2008).
- [53] V. M. Silkin, A. Balassis, P. M. Echenique, and E. V. Chulkov, *Phys. Rev. B* **80**, 054521 (2009).
- [54] J. P. Echeverry, E. V. Chulkov, P. M. Echenique, and V. M. Silkin, *Phys. Rev. B* **85**, 205135 (2012).
- [55] M. N. Faraggi, A. Arnau, and V. M. Silkin, *Phys. Rev. B* **86**, 035115 (2012).
- [56] P. Cudazzo, M. Gatti, and A. Rubio, *Phys. Rev. B* **86**, 075121 (2012).
- [57] P. Cudazzo, M. Gatti, and A. Rubio, *Phys. Rev. B* **90**, 205128 (2014).
- [58] P. Cudazzo and M. Gatti, *Phys. Rev. B* **96**, 125131 (2017).
- [59] M. Petersilka, U. J. Gossmann, and E. K. U. Gross, *Phys. Rev. Lett.* **76**, 1212 (1996).
- [60] E. H. Hygh and R. M. Welch, *Phys. Rev. B* **1**, 2424 (1970).
- [61] O. Jepsen, *Phys. Rev. B* **12**, 2988 (1975).
- [62] I. Bakonyi, H. Ebert, and A. I. Liechtenstein, *Phys. Rev. B* **48**, 7841 (1993).
- [63] M. Sanati, A. Saxena, T. Lookman, and R. C. Albers, *Phys. Rev. B* **63**, 224114 (2001).
- [64] M. Jafari and H. R. Hajiyani, *Comp. Mater. Sci.* **50**, 2549 (2011).
- [65] V. M. Silkin, A. Garcia-Lekue, J. M. Pitarke, E. V. Chulkov, E. Zaremba, and P. M. Echenique, *Europhys. Lett.* **66**, 260 (2004).
- [66] B. Diaconescu, K. Pohl, L. Vattuone, L. Savio, P. Hofmann, V. M. Silkin, J. M. Pitarke, E. V. Chulkov, P. M. Echenique, and M. Rocca, *Nature (London)* **448**, 57 (2007).
- [67] S. J. Park and R. E. Palmer, *Phys. Rev. Lett.* **105**, 016801 (2010).
- [68] H. Pfnür, T. Langer, J. Baringhaus, and C. Tegenkamp, *J. Phys.: Condens. Matter* **23**, 112204 (2011).
- [69] M. Jahn, M. Müller, M. Endlich, N. Néel, J. Kröger, V. Chis, and B. Hellsing, *Phys. Rev. B* **86**, 085453 (2012).
- [70] J. Pischel, E. Welsch, O. Skibbe, and A. Pucci, *J. Phys. Chem. C* **117**, 26964 (2013).

- [71] X. Jia, S. Y. Zhang, R. Sankar, F. C. Chou, W. H. Wang, K. Kempa, E. W. Plummer, J. D. Zhang, X. T. Zhu, and J. D. Guo, *Phys. Rev. Lett.* **119**, 136805 (2017).
- [72] A. Politano, H. K. Yu, D. Farias, and G. Chiarello, *Phys. Rev. B* **97**, 035414 (2018).
- [73] D. W. Lynch, C. G. Olson, and J. H. Weaver, *Phys. Rev. B* **11**, 3617 (1975).
- [74] E. E. Krasovskii and V. N. Antonov, *Int. J. Mod. Phys. C* **2**, 400 (1991).
- [75] Y. Takada and H. Yasuhara, *Phys. Rev. Lett.* **89**, 216402 (2002).
- [76] G. G. Fuentes, I. G. Mancheño, F. Balbás, C. Quirós, J. F. Trigo, F. Yubero, E. Elizalde, and J. M. Sanz, *Phys. Status Solidi A* **175**, 429 (1999).
- [77] P. Prieto, F. Yubero, E. Elizalde, and J. M. Sanz, *J. Vac. Sci. Technol. A* **14**, 3181 (1996).
- [78] J. C. Ingram, K. W. Nebesny, and J. E. Pemberton, *Appl. Surf. Sci.* **45**, 247 (1990).
- [79] G. W. Simmons and E. J. Scheibner, *J. Appl. Phys.* **43**, 693 (1972).
- [80] F. Pellerin and J. P. Langeron, *Surf. Sci.* **126**, 444 (1983).
- [81] B. M. Biwer and S. L. Bernasek, *Surf. Sci.* **167**, 207 (1987).
- [82] E. Bertel, R. Stockbauer, and T. E. Madey, *Surf. Sci.* **141**, 355 (1984).
- [83] P. Bracconi and R. Lässer, *Appl. Surf. Sci.* **28**, 204 (1987).
- [84] J. Frandon, B. Brousseau, and F. Pradal, *Phys. Status Solidi B* **98**, 379 (1980).
- [85] E. A. Bakulin, L. A. Balabanova, M. M. Bredov, E. G. Ostroumova, E. V. Stepin, and V. V. Shcherbinina, *Sov. Phys. Solid State* **11**, 549 (1969).
- [86] N. G. Alexandropoulos, G. Bambakidis, T. Sparrow, and B. Williams, *J. Phys. F* **16**, L245 (1986).
- [87] W. K. Schubert, R. N. Shelton, and E. L. Wolf, *Phys. Rev. B* **24**, 6278 (1981).
- [88] O. T. Woo and G. J. C. Carpenter, *Microsc. Microanal. Microstruct.* **3**, 35 (1992).
- [89] K. O. Axelsson, K. E. Kech, and B. Kasemo, *Surf. Sci.* **164**, 109 (1985).
- [90] G. R. Corallo, D. A. Asbury, R. E. Gilbert, and G. B. Hoflund, *Phys. Rev. B* **35**, 9451 (1987).
- [91] P. Aebi, M. Erbudak, A. Leonardi, and F. Vanini, *J. Electron Spectrosc. Relat. Phenom.* **42**, 351 (1987).
- [92] Z. Zhao, J.-P. Morniroli, A. Legris, A. Ambard, Y. Kihn, L. Legras, and M. Blat-Yrieix, *J. Microscopy* **232**, 410 (2008).
- [93] M. J. Lynch and J. B. Swan, *Aust. J. Phys.* **21**, 811 (1968).
- [94] X. Zubizarreta, V. M. Silkin, and E. V. Chulkov, *Phys. Rev. B* **90**, 165121 (2014).
- [95] D. A. Papaconstantopoulos and A. C. Switendick, *J. Less-Common Met.* **103**, 317 (1984).
- [96] E. E. Krasovskii, V. V. Nemoshkalenko, G. F. Kobzenko, and V. N. Antonov, *Int. J. Hydrogen Energy* **20**, 373 (1995).
- [97] V. M. Silkin, I. P. Chernov, P. M. Echenique, Y. M. Koroteev, and E. V. Chulkov, *Phys. Rev. B* **76**, 245105 (2007).
- [98] B. C. Lamartine, T. W. Haas, and J. S. Solomon, *Appl. Surf. Sci.* **4**, 537 (1980).
- [99] J. M. Sanz, D. Ortiz, R. Alcaraz de la Osa, J. M. Saiz, F. González, A. S. Brown, M. Losurdo, H. O. Everitt, and F. Moreno, *J. Phys. Chem. C* **117**, 19606 (2013).